

RESEARCH ARTICLE

Two-in-one shell configuration for bimetal selenides toward fast sodium storage within broadened voltage windows

Zichao Yan¹  | Lingfei Zhao² | Yaru Liang³ | Lei Zhang¹ | Hanwen Liu² | Zhiqiang Zhu¹ | Yunxiao Wang² | Shu-Lei Chou⁴

¹State Key Laboratory of Chemo/Biosensing and Chemometrics, College of Chemistry and Chemical Engineering, Hunan University, Changsha, China

²Institute for Superconducting & Electronic Materials, University of Wollongong, Innovation Campus, North Wollongong, New South Wales, Australia

³School of Materials Science and Engineering, Xiangtan University, Hunan, Xiangtan City, China

⁴Institute for Carbon Neutralization, College of Chemistry and Materials Engineering, Wenzhou University, Wenzhou, Zhejiang, China

Correspondence

Zhiqiang Zhu, State Key Laboratory of Chemo/Biosensing and Chemometrics, College of Chemistry and Chemical Engineering, Hunan University, 410082 Changsha, China.
Email: zqzhu@hnu.edu.cn

Shu-Lei Chou, Institute for Carbon Neutralization, College of Chemistry and Materials Engineering, Wenzhou University, Wenzhou, 325035 Zhejiang, China.
Email: chou@wzu.edu.cn

Funding information

Fundamental Research Funds for the Central Universities, Grant/Award Numbers: 531118010111, 531118010633; National Natural Science Foundation of China, Grant/Award Numbers: 22109041, 52103313

Abstract

The shell structure design has been recognized as a highly efficient strategy to buffer the severe volume expansion and consecutive pulverization of conversion-type anodes. Nevertheless, construction of a functional shell with a stabilized structure that meets the demands of both high electronic conductivity and feasible pathways for Na⁺ ions has been a challenge so far. Herein, we design a two-in-one shell configuration for bimetal selenides to achieve fast sodium storage within broadened voltage windows. The hybridized shell, which benefits from the combination of titanium dioxide quantum dots and amorphous carbon, can not only effectively buffer the strain and maintain structural integrity but also allow facile and reversible transport of electrons and Na⁺ uptake for electrode materials during sodiation/desodiation processes, resulting in increased reaction kinetics and diffusion of sodium ions, conferring many benefits to the functionality of conversion-type electrode materials. As a representative material, Ni-CoSe₂ with such structural engineering shows a reversible capacity of 515 mAh g⁻¹ at 0.1 A g⁻¹ and a stable capacity of 416 mAh g⁻¹ even at 6.4 A g⁻¹; more than 80% of the capacity at 0.1 A g⁻¹ could be preserved, so that this strategy holds great promise for designing fast-charging conversion-type anodes in the future.

KEYWORDS

bimetal selenides, fast charging, hybridized shell, sodium-ion batteries, structure engineering

This is an open access article under the terms of the Creative Commons Attribution License, which permits use, distribution and reproduction in any medium, provided the original work is properly cited.

© 2022 The Authors. *Carbon Energy* published by Wenzhou University and John Wiley & Sons Australia, Ltd.

1 | INTRODUCTION

With the shortage of Li resources, the idea of using novel energy storage systems (ESSs) with reasonable cost and performance is becoming popular.¹ Recently, the interest in commercializing new ESSs to meet the increasing demands has rationally extended to Na-based systems since the introduction of electronic products that are powered by sodium-ion batteries (SIBs).^{2,3} Nevertheless, the features of sodium present sluggish reaction kinetics and lower energy density in electrochemical storage compared to those of lithium (radius: 0.113 nm/0.076 nm; mass: 22.99 g mol⁻¹/6.94 g mol⁻¹; potential: -2.71 V/-3.04 V vs. E^o, corresponding to Na and Li, respectively).⁴⁻⁶ It is, therefore, very important to exploit high-capacity electrode materials with fast reaction kinetics to broaden their potential applications.^{7,8}

Transition-metal selenides are promising anode materials for SIBs due to their high theoretical capacity and Na⁺ insertion/extraction channels. Compared to their oxide and sulfide counterparts, transition-metal selenides not only present narrow band gaps with good conductivity but also show lower reaction energy barriers.^{5,9-11} However, just as most conversion-type electrodes, transition-metal selenides also have the disadvantages of irreversible intermediates and side reactions under low discharge potential, resulting in rapid capacity decay and poor reversible capacity. Besides, the potential windows of the majority of monometallic selenides have to be constrained to 0.5–3.0 V to achieve stable cycling and rate capability. Taking CoSe₂ as an example, the discharge potential region below 0.4 V will cause pulverization and structural damage as well as an irreversible topotactic reaction due to the deep conversion reaction of the CoSe

intermediate and the strong Jahn–Teller effect of the low-spin electronic structure $t_{2g}^6e_g^1$ of Co 3d electrons.^{12,13} Thus, the cut-off voltage (0.5–3 V) is generally increased to avoid the irreversible degradation of transition-metal selenides, which, however, would adversely affect their practical capacities.¹⁴ To overcome this problem, Jiang et al.¹⁵ and Yousaf et al.¹⁶ proposed that the bimetal selenides can partly alleviate the Jahn–Teller distortion of Co²⁺ and broaden the voltage window, but deep conversion would still cause severe volume expansion and consecutive pulverization with subsequent side reactions (electrolyte consumption, electrode cracks, and formation of compact electrolyte interphase films), leading to sluggish reactivity and accelerated capacity fading at high rates. Therefore, it would be challenging but highly profitable to realize fast and stable sodium storage of bimetal selenides within broadened voltage windows.

Structural engineering is one of the most effective strategies to improve the sodium storage performance of electrode materials.¹⁷⁻²³ For example, the design of a functional carbon shell could lead to good electrochemical performance by suppressing volume expansion, enhancing electricity, and preventing dissolution for a variety of conversion-type electrode materials, such as S, CoO, Cu₂S, Sn, and so forth.²⁴⁻²⁷ As shown in Figure 1A, this strategy, however, pays little attention to the reaction kinetics; for example, the pathways of Na⁺ ions in the disordered structure of amorphous carbon layers are rarely mentioned, even though the sodiation/desodiation of Na⁺ ions might be retarded by them.²⁸ Meanwhile, on the basis of inducing a high ionic conductive coating layer, a multishell design integrating the merits of individual layers has been proposed.²⁶ As shown in Figure 1B, with increasing layer number, there will be

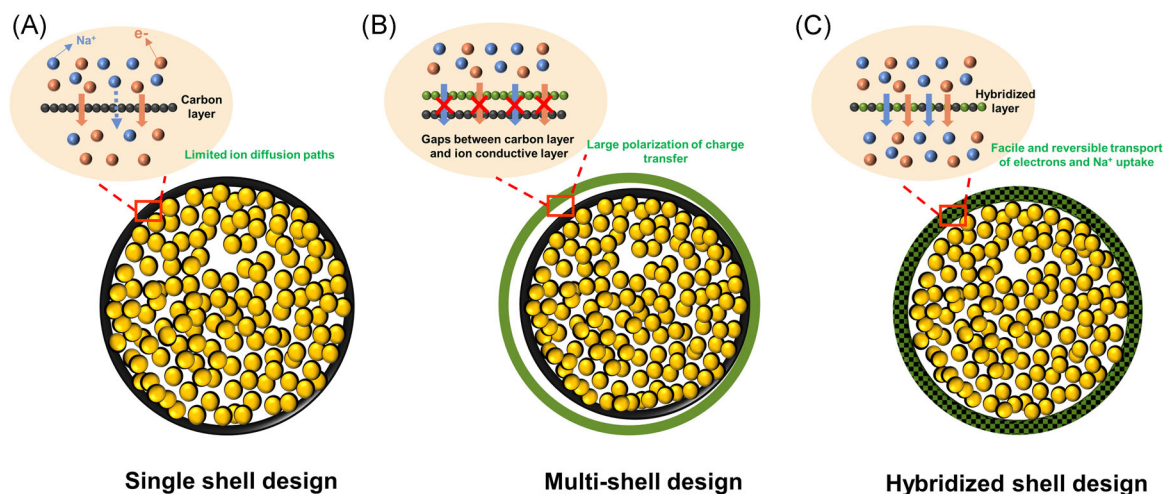


FIGURE 1 Schematic of the materials design for (A) a single shell, (B) multishells, and (C) a hybridized shell

gaps and limited contact area between each shell, which would not favor the ion diffusion paths, due to the disordered migration path and electric field.^{29,30} Thermodynamically, the limited contact area may also induce large polarization of charge transfer according to the following equation³¹:

$$\eta = kiS/r, \quad (1)$$

where η is the potential of a charge, k is the electrostatic force constant, i is the current density, S represents the contact area, and r is the distance between this charge and the point charge. Then, reducing S can lead to higher electron-transfer barrier. Thus, as shown in Figure 1C, creating a hybridized shell by coupling components with high electronic and ionic conductivity is strongly believed to be a good way to accommodate the conversion-type bimetal selenides for fast and stable sodium storage within broadened voltage windows.

On proof of this concept, herein, we report a two-in-one shell configuration of carbon and titanium dioxide for bimetal selenides to achieve fast and stable sodium storage within broadened voltage windows. Titanium dioxide quantum dots with high ionic conductivity and the “zero-strain” characteristic are expected to allow fast pass-through and uptake of Na^+ without degrading the structure,^{32–34} while the conductive amorphous carbon could construct a fast electric path.³⁵ Therefore, the structurally engineered Ni-CoSe₂ anode, integrating the merits of titanium dioxide quantum dots/amorphous carbon hybridized shell (Ni-CoSe₂@TQDs/AC), can not only effectively buffer the strain and maintain the structural integrity but also allow fast and reversible transport of electrons/ions, resulting in increased reaction kinetics and high rate of Na storage.

2 | EXPERIMENTAL SECTION

2.1 | Materials synthesis

2.1.1 | Synthesis of ZIF-67

First, cobalt nitrate (0.29 g) was dissolved in 25 mL of methanol (solution A), and 2-methylimidazole (0.33 g) was dissolved in 25 mL of methanol (solution B). Then, solution B was immediately poured into solution A. The mixed solution was left to stand for 24 h at room temperature. The obtained precursor solution was washed with methanol three times and dried at 70°C overnight.

2.1.2 | Synthesis of bimetallic zeolitic imidazolate frameworks (BM-ZIFs)

40 mg of the obtained ZIF-67 was dispersed in 25 mL of ethanol by 30 min of ultrasonic dispersion. Then, 60 mg of nickel nitrate was added into the above solution. The mixed solution was stirred for 30 min at room temperature. The obtained precursor solution was washed with ethanol three times and dried at 70°C overnight.

2.1.3 | Synthesis of Ni-CoSe₂@TQDs/AC

60 mg of the obtained BM-ZIFs was dispersed in 50 mL of ethanol with the addition of 0.15 mL of ammonium hydroxide and 30 mg of hexadecylamine (solution A), and 30 μL of isopropyl titanate was dissolved in 10 mL of ethanol (solution B). Then, solution B was dropped into solution A. The mixed solution was stirred for 1 h at room temperature. The obtained precursor solution was washed with methanol and dried at 70°C overnight. 40 mg of the dried product were further dispersed in 20 mL of ethanol with the addition of 35 mg of resorcinol, 40 μL of ammonium hydroxide, and 60 μL of distilled water. Then, 50 μL of formalin solution was added to the above solution, which was stirred for 6 h, aged overnight at 35°C, and washed with ethanol three times. Finally, the obtained precursor was ground with selenium powder (weight ratio 1:1) and then calcined at 600°C for 2.5 h to obtain the final composite.

2.1.4 | Synthesis of Ni-CoSe₂@AC

40 mg of the obtained BM-ZIFs were dispersed in 20 mL of ethanol with the addition of 35 mg of resorcinol, 40 μL of ammonium hydroxide, and 60 μL of distilled water. Then, 50 μL of formalin solution was added to the above solution, which was stirred for 6 h, aged overnight at 35°C, and washed with ethanol three times. Finally, the obtained precursor was ground with selenium powder (weight ratio 1:1) and then calcined at 600°C for 2.5 h to obtain the final composite.

2.1.5 | Synthesis of Ni-CoSe₂

40 mg of the obtained BM-ZIFs were ground with selenium powder (weight ratio 1:1) and then calcined at 600°C for 2.5 h to obtain the final composite.

2.2 | Materials characterization

X-ray diffraction (XRD) patterns were obtained with Cu K α radiation in the 2θ range of 10° – 70° (PANalytical diffractometer, $\lambda = 1.5406 \text{ \AA}$, step size of $0.02^\circ \text{ s}^{-1}$). The morphology was detected using a field emission scanning electron microscope (FESEM; JEOL JSM-7500FA). A 200 kV scanning transmission electron microscope (STEM; JEM-ARM 200F) was equipped with a double-aberration corrector to achieve selected area electron diffraction with a probe-forming, image-forming lens systems. The angular range of collected electrons for the high-angle annular dark-field images was around 70 – 250 mrad , while annular bright-field (ABF)-STEM images were recorded using an STEM-ABF detector simultaneously. The energy-dispersive spectroscopy (EDS) mapping results were obtained via STEM using NSS software. In situ nanofabrication in this study was carried out inside a transmission electron microscope (TEM; FEIT Tecnai F20st) using a TEM-STM holder (Pico Femto FE02-ST) from Zeptools Co., Ltd. X-ray photoelectron spectroscopy (XPS) with Al K α radiation ($h\nu = 1486.6 \text{ eV}$) was used to detect the binding energies using a SPECSPHOIBOS 100 Analyser installed in a high-vacuum chamber. The porosity was measured by nitrogen sorption isotherms at 77 K using a Micromeritics Tristar 3020 analyzer. Raman spectra were collected using a 10 mW helium/neon laser at 632.8 nm excitation (which was filtered by a neutral density filter to reduce the laser intensity) and a charge-coupled detector (CCD). The thermal decomposition behavior of the products was monitored using a Mettler Toledo TGA/SDTA851 analyzer from 50°C to 800°C in argon at a heating rate of $5^\circ\text{C}/\text{min}$.

2.3 | Electrochemical measurements

The working electrodes for sodium-ion cells were fabricated by mixing the as-synthesized samples, carbon black, and carboxymethyl cellulose binder in a weight ratio of 70:20:10 in water, which were then pasted on copper foil, followed by drying under vacuum at 80°C overnight. The test cells were assembled with metallic sodium as the negative electrode, a glass fiber separator (Whatman GF/F), and 1 M NaClO_4 in 1:1 (volume/volume) ethylene carbonate/propylene carbonate with 3 wt% fluoroethylene carbonate additives (PC/EC + 3 wt% FEC) as an electrolyte. The assembly of the test cells was carried out in an argon-filled glovebox, where water and oxygen concentrations were kept at less than 0.1 ppm . The electrochemical properties were examined using a NEWARE test system over a voltage range from

0.01 to 3 V (vs. Na/Na^+). Cyclic voltammetry and impedance testing were performed using a Biologic VMP-3 electrochemical workstation from 0.01 to 3 V .

3 | RESULTS AND DISCUSSION

The synthetic process for the structurally engineered Ni-CoSe $_2$ @TQDs/AC is schematically illustrated in Figure 2. The introduced Ni $^{2+}$ ions will partially replace the original Co $^{2+}$ ions of zeolitic imidazolate frameworks, and the BM-ZIF precursor is thereby realized. Afterward, the precursor is uniformly coated with a hexadecylamine–titania oligomer composite (HDA/TO) and resorcinol/formaldehyde (RF) resins. The amino groups in the HDA molecules can interact with the titania oligomers by hydrogen bonding to build a uniform titania-based hydrophilic surface where resorcinol/formaldehyde polymerization is favored. During the carbonization and selenylation process, the HDA/TO and RF layers gradually evolve into a hybrid TQDs/AC shell with the HDA molecules evaporated under the high temperature. Because they are subjected to growth in confined spaces and molecularly mediated effects, the titania oligomers tend to grow into quantum dots, mediated by the HDA molecules and confinement by the RF resins.

As characterized by FESEM (Figure 3A–C), the obtained Ni-CoSe $_2$ @TQDs/AC nanocages are highly uniform, with an average size of about 650 nm . Both Ni-CoSe $_2$ and Ni-CoSe $_2$ @AC were synthesized using similar procedures to that of Ni-CoSe $_2$ @TQDs/AC (as detailed in the Section 2). The corresponding FESEM and STEM images are shown in Figure S1, which confirm their morphologies. The TEM images in Figure 3D,E show that the TQDs/AC coverage maintained its thickness of about 15 nm and some void spaces inside the nanocages were generated after the evaporation of organic linkers during the carbonization and selenylation process. The void space can well buffer the strain of Ni-CoSe $_2$, while the shell structure can prevent the escape of active material during charging/discharging. The high-resolution TEM image in Figure 3F further reveals that the shell of TiO $_2$ quantum dots embedded inside the amorphous carbon layer is in close contact with the Ni-CoSe $_2$ nanoparticles, which should favor the transport of electrons and offer abundant active sites for Na $^+$ uptake. In addition, the STEM-EDS mapping of Ni-CoSe $_2$ @TQDs/AC shows the homogeneous distribution of TQDs along with the AC layer, demonstrating the successful integration of TQDs and AC in the hybridized shell (Figure 3G).

The XRD pattern of Ni-CoSe $_2$ is in good agreement with that of the standard cubic CoSe $_2$ (PDF# 65-3327) (Figure 4A). The phase purity is also retained for the AC- and TQDs/AC-coated samples. There are two small peaks located at 27.4° and 36.1° for Ni-CoSe $_2$ @TQDs/

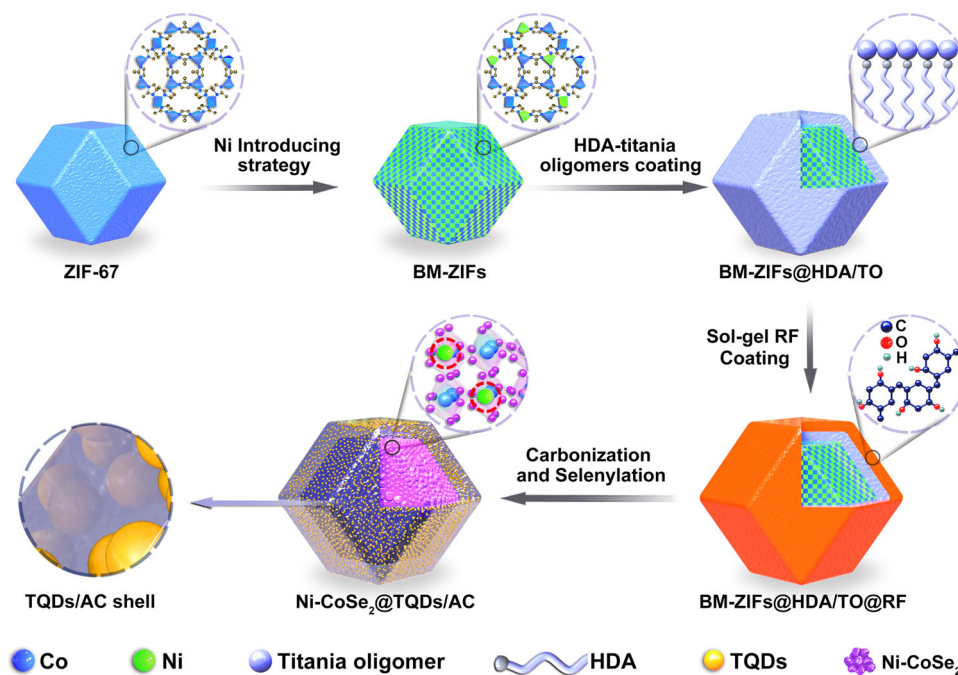


FIGURE 2 Schematic illustration of the synthesis process for Ni-CoSe₂@TQDs/AC. BM-ZIF, bimetallic zeolitic imidazolate framework; HDA, hexadecylamine; RF, resorcinol/formaldehyde; TQDs/AC, titanium dioxide quantum dots/amorphous carbon hybridized shell

AC, which can be assigned to the (110) and (101) planes of rutile TiO₂ (PDF# 75-1752), respectively. The Raman analysis clearly confirmed the structural properties of the Ni-CoSe₂, TQDs, and AC (Figure 4B). All the samples showed five obvious peaks, which were located at approximately 189, 676, 513, 1344, and 1602 cm⁻¹. The first three peaks correspond to the lattice vibrational modes of Ag for CoSe₂, A_{1g} for CoSe₂, and E_g for CoO-Co₃O₄, respectively, due to the minor oxidation of Co by a slight amount of SeO₂ in the Se source.^{5,30} The latter two peaks are assigned to the general D and G bands of the amorphous carbon generated from RF resins and ZIFs.^{36,37} A newly observed peak located at 399 cm⁻¹ in Ni-CoSe₂@TQDs/AC can be attributed to the B_{1g} mode of TiO₂.³⁸ These results confirm that the TQDs/AC layer and the introduction of moderate Ni do not cause any changes in the local structure of cubic CoSe₂.

The elemental composition and valence bond analysis of Ni-CoSe₂@TQDs/AC were investigated by XPS. The elements Ni, Co, Se, Ti, N, and C were characterized by the survey spectrum, and it is worth noting that the N element can be assigned to the N-doped carbon generated from the ZIFs (Figure 4C). As shown in Figure 4D, the high-resolution XPS spectra of Co 2p contains six fitted peaks for Co 2p_{3/2}, Co 2p_{1/2}, and satellite peaks of Co 2p. The peaks observed at 778.4 and 793.5 eV are assigned to the Co 2p_{3/2} and Co 2p_{1/2} peaks of CoSe₂, respectively, and those with binding energies of 781.0 and 796.50 eV are indexed to the Co-O bands of

the native oxide layers at the surface,³⁹ which is in accordance with the detected oxides in the Raman spectrum. The high-resolution XPS spectrum of Ni 2p equally contains information showing Ni-Se (853.3 and 870.5 eV) and Ni-O (855.1 and 873.4 eV) bonding,⁴⁰ which confirms that the Ni was successfully introduced into the CoSe₂ local structure (Figure 4E). This is also consistent with the Se 3d peaks of Ni-CoSe₂@TQDs/AC, in which the Se 3d_{3/2} (55.8 eV) and Se 3d_{5/2} (54.6 eV) peaks are consistent with the previously reported binding energies between Se anions and metal cations (Figure 4F).¹¹ The weak peak at 59.3 eV was assigned to Se-O/Se-C bonding structures at the surface. Notably, Figure 4G demonstrates that the 2p peaks of Ti are located at 458.0 and 463.8 eV, which can be attributed to Ti⁴⁺, evidencing the successful formation of TiO₂ in the hybridized shell.⁴¹

To further explore the element contents in Ni-CoSe₂@TQDs/AC, EDS spectroscopy was used to study the metallic elements. The atomic weights of Ni, Co, and Ti, as evaluated by the EDS spectrum, are 3.10%, 13.05%, and 3.05%, respectively, implying the 1:4 molar ratio of Ni to Co and that there are 5 wt% TQDs in the Ni-CoSe₂@TQDs/AC (Figure S2). The stoichiometry of the as-synthesized Ni-CoSe₂ was further determined by inductively coupled plasma analysis to verify the composition. As shown in Table S1, the measurement result shows that the Ni-CoSe₂ molar ratio is 1:3.96, which is very close to the EDS result. For the carbon content, the thermogravimetric analysis of all the

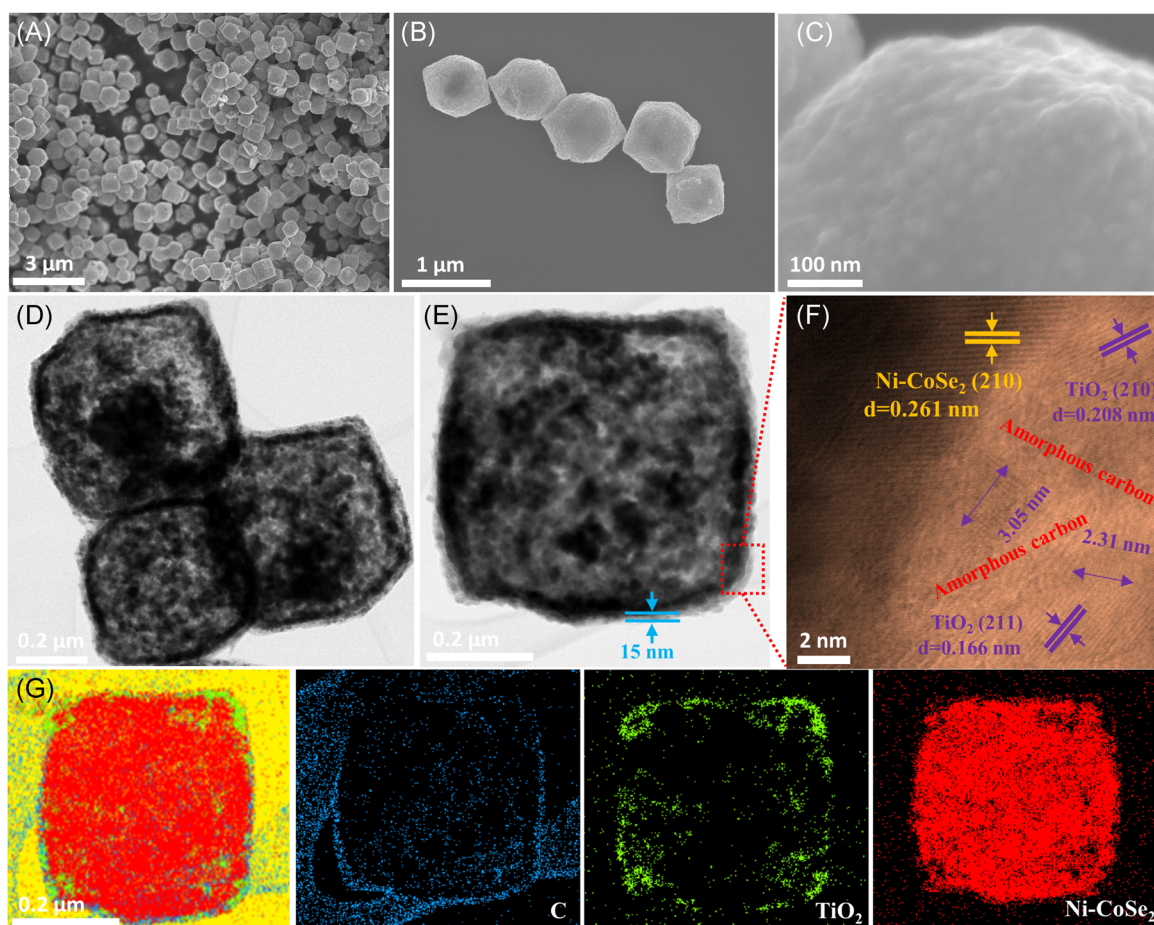


FIGURE 3 (A–C) Field emission scanning electron microscope image, (D,E) transmission electron microscope image, (F) high-resolution transmission electron microscope image, and (G) scanning transmission electron microscope–energy-dispersive spectroscopy mapping of the Ni-CoSe₂@TQDs/AC nanocages. TQDs/AC, titanium dioxide quantum dots/amorphous carbon hybridized shell

samples showed weight loss of around 70%, which can be attributed to the carbon from the ZIFs-derived carbon matrix and AC shell and the conversion from Ni-CoSe₂ into Co₃O₄ and NiO (Figure 4H,I). Thus, the calculated carbon contents in Ni-CoSe₂ and Ni-CoSe₂@AC based on Equation (2) are 19 and 29 wt%, respectively, implying the 10 wt% weight ratio of the AC shell.

obvious capacity decay in the initial cycle can be mainly attributed to the decomposition of the electrolyte and the establishment of a solid-electrolyte interphase layer over the electrode surface.^{42–44} In comparison, the shell-free Ni-CoSe₂ delivered similar capacity for the first cycle, but which sharply decreased to 276 mAh g⁻¹ in the following 100 cycles. The shell-free Ni-CoSe₂ electrode also showed

$$\text{Carbon content (wt\%)} = 1 - \frac{15 \times \text{molecular wt of Ni}_{0.2}\text{Co}_{0.82}\text{Se}_2 \times \text{final wt of Co}_3\text{O}_4 \text{ and NiO}}{3 \times \text{molecular wt of NiO} + 4 \times \text{molecular wt of Co}_3\text{O}_4} \quad (2)$$

The superior sodium storage performance of the two-in-one shell-engineered Ni-CoSe₂ is shown in Figure 5. For comparison, Ni-CoSe₂ and Ni-CoSe₂@AC were also tested. Both the Ni-CoSe₂@AC and the Ni-CoSe₂@TQDs/AC composites showed highly reversible capacities in the voltage window of 0.01–3 V, which delivered an initial capacity of about 650 mAh g⁻¹ and maintained a stable capacity of about 453 mAh g⁻¹ for the subsequent 100 cycles at a current density of 0.2 A g⁻¹ (Figure 5A). The

a steep plateau with increasing cycle number and a relatively larger polarization value of 730 mV at the second cycle, and this value even increased to 988 mV by the 100th cycle (Figure 5B). On increasing the current density to 1 A g⁻¹, the shell-free sample showed a sharp capacity decay after 30 cycles, indicating much worse cycling stability compared to the other two samples (Figure S3). The improved cycling stability and reduced polarization of Ni-CoSe₂@AC and Ni-CoSe₂@TQDs/AC

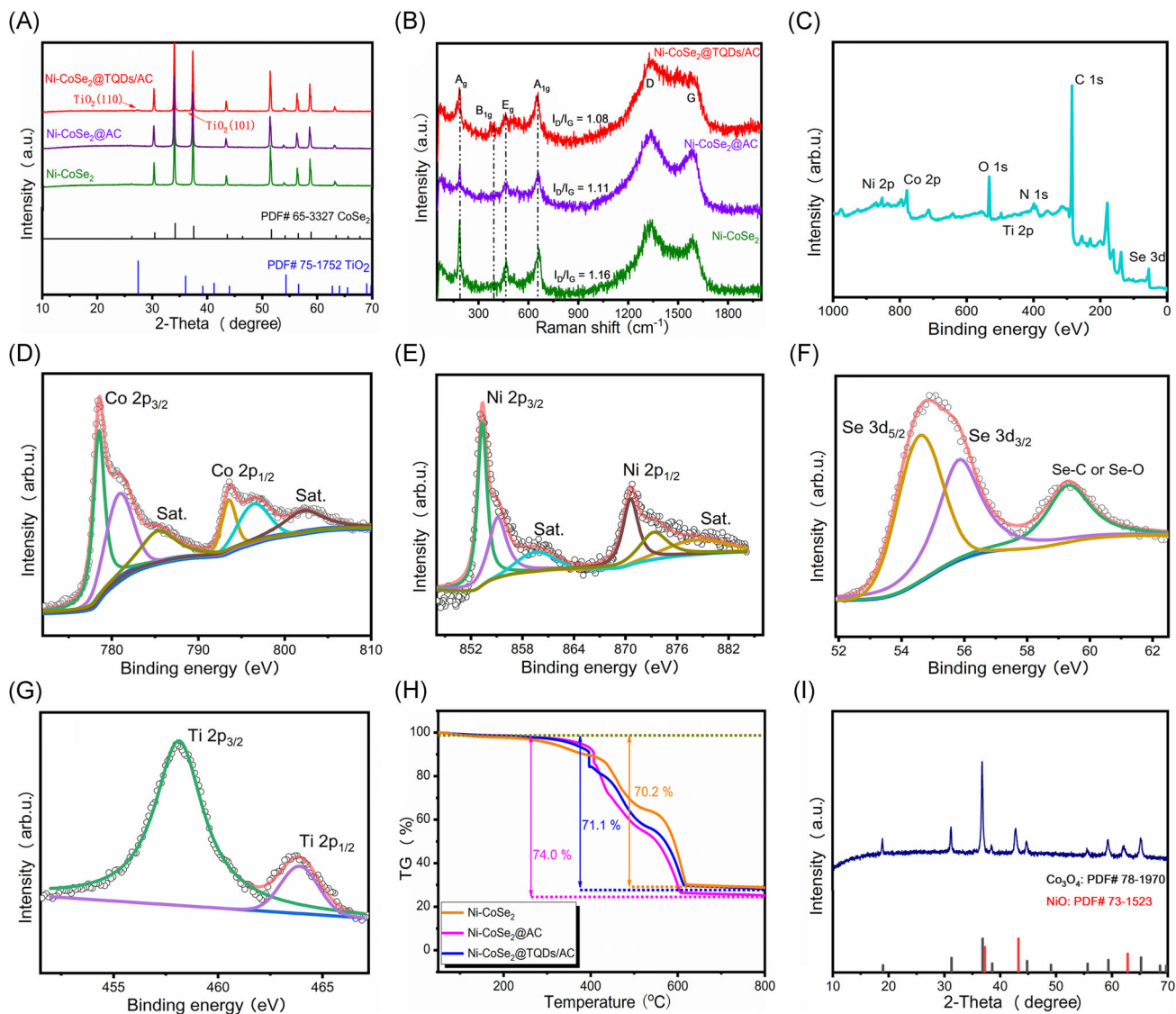


FIGURE 4 (A) XRD pattern and (B) Raman spectrum of the Ni-CoSe₂, Ni-CoSe₂@AC, and Ni-CoSe₂@TQDs/AC. (C) XPS survey and high-resolution spectra of (D) Co 2p, (E) Ni 2p, (F) Se 3d, and (G) Ti 2p for Ni-CoSe₂@TQDs/AC. (H) TGA curve of the Ni-CoSe₂, Ni-CoSe₂@AC, and Ni-CoSe₂@TQDs/AC. (I) XRD pattern of the TGA residue for Ni-CoSe₂. TQDs/AC, titanium dioxide quantum dots/amorphous carbon hybridized shell; TGA, thermogravimetric analysis; XPS, X-ray photoelectron spectroscopy; XRD, X-ray diffraction

are likely attributable to the engineered shell, which is beneficial to improving the structure integrity and conductivity of Ni-CoSe₂ over a wide voltage range. The capability of TQD-active sites for Na⁺ uptake has been evaluated under high-rate testing. Figure 5C shows the sodium storage performances of the three samples at different current densities. Excitingly, Ni-CoSe₂@TQDs/AC presented excellent rate performance, delivering reversible capacities of 515–416 mAh g⁻¹ at current densities from 0.1 to 6.4 A g⁻¹, respectively, corresponding to a capacity retention of more than 80% of the capacity at 0.1 A g⁻¹. In comparison, on increasing the current density from 0.1 to 6.4 A g⁻¹, the reversible capacity of Ni-CoSe₂ and Ni-CoSe₂@AC decreased from

535/517 to 198/354 mAh g⁻¹, corresponding to a poor capacity retention of 37% and 68%, respectively. Their charge/discharge platforms were clearly shortened, and the polarization became obvious with increasing current density, so that Ni-CoSe₂@TQDs/AC maintained the best performance among them, implying an intact structure and a facile diffusion rate of sodium ions during the high-rate testing (Figure 5D–F). As shown in Figure 5G, our material can achieve a capacity of 416 mAh g⁻¹ at a current density of 6.4 A g⁻¹ with capacity retention of more than 80%, which is much higher than that in previous studies with discharge capacities of around 300 mAh g⁻¹. Besides, the Ni-CoSe₂@TQDs/AC anode maintained a stable capacity of 453 mAh g⁻¹ after 100

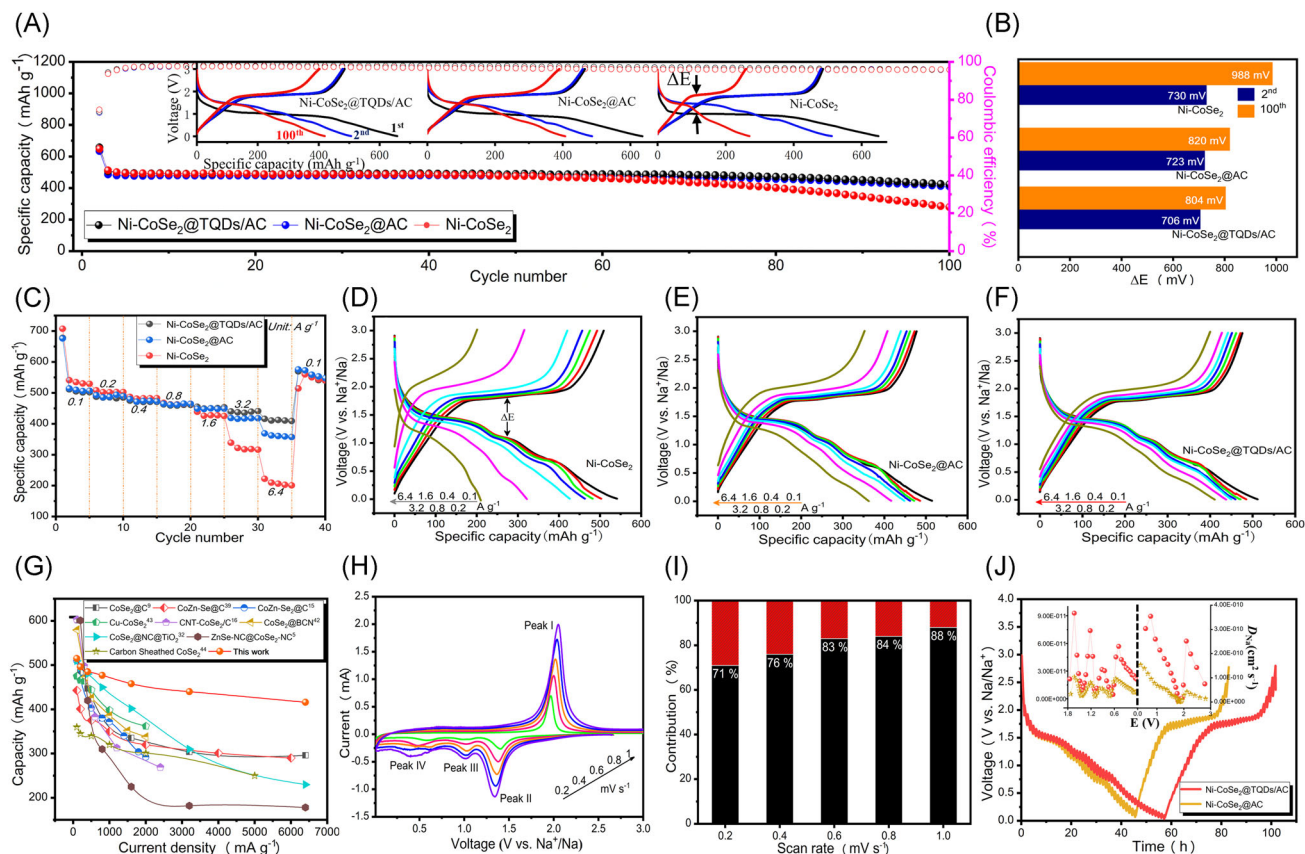


FIGURE 5 Comparison of (A) the cycling performances of the samples with the corresponding charge/discharge curves (insets) at 0.2 A g^{-1} , (B) polarization values in different cycles, (C) rate performances from 0.1 to 6.4 A g^{-1} , and (D–F) charge/discharge curves at different rates for Ni-CoSe_2 , $\text{Ni-CoSe}_2@\text{AC}$, and $\text{Ni-CoSe}_2@\text{TQDs/AC}$. (G) Performance comparison of the materials in this study with previously reported metal/bimetal selenides with respect to the rate capability. (H) CV curves at various scan rates from 0.2 to 1 mV s^{-1} and (I) the ratios of the capacitive contributions to the total capacity at various scan rates of $\text{Ni-CoSe}_2@\text{TQDs/AC}$. (J) GITT charge/discharge curves of $\text{Ni-CoSe}_2@\text{TQDs/AC}$ and $\text{NiCoSe}_2@\text{AC}$ with the calculated D_{Na} as the inset. CV, cyclic voltammogram; GITT, galvanostatic intermittent titration technique; TQDs/AC, titanium dioxide quantum dots/amorphous carbon hybridized shell

cycles at a current density of 0.2 A g^{-1} with a capacity retention of 90% relative to the second cycle, which is about a 14% improvement in capacity retention and 22% enhancement in the specific capacity of the published metal selenide-based anodes.^{9,10} To the best of our knowledge, this rate performance with a conventional current collector and a carbonate-based electrolyte, benefitting from the integrated titanium dioxide quantum dots and an amorphous carbon shell, has competitive high-rate cycling stability for SIBs. Furthermore, a detailed kinetic analysis of $\text{Ni-CoSe}_2@\text{TQDs/AC}$ for ultrafast sodium storage was conducted using cyclic voltammograms (CVs) and the galvanostatic intermittent titration technique (GITT). The CV curves of $\text{Ni-CoSe}_2@\text{TQDs/AC}$ show similar outlines and well-preserved redox peaks at different scan rates, indicating the weak polarization (Figure 5H). There are three obvious cathodic peaks located at 1.42, 1.01, and 0.49 V, corresponding to the conversion of Na_xCoSe_2 , CoSe, and

Co, respectively, which are in good agreement with the charge/discharge platforms.⁹ The functional relationship between the peak current (i) and the sweep rate (v) of the four redox peaks was qualitatively analyzed according to a power-law equation: $i = av^b$, wherein a and b are adjustable parameters and calculable by plotting $\log(i)$ versus $\log(v)$.^{34,45,46} As shown in Figure S4, the calculated b values of peaks I–IV are 0.67, 0.91, 0.93, and 0.81, respectively, indicating a sodium storage process that is co-controlled by diffusion and pseudocapacitive behavior in the $\text{Ni-CoSe}_2@\text{TQDs/AC}$ electrode. The capacitive proportions are further quantitatively differentiated as $\sim 71.3\%$ at 0.2 mV s^{-1} and finally reached 88% at 1 mV s^{-1} (Figure 5I), based on a power-law equation¹⁸: $i = k_1v + k_2v^{1/2}$, where k_1v and $k_2v^{1/2}$ represent the capacitive and diffusion contributions, respectively, implying a fast Na^+ sodiation/desodiation process for enhanced cycling stability and rate capability.⁴⁴ In addition, the Na^+ diffusivity (D_{Na^+}) of the $\text{Ni-CoSe}_2@\text{TQDs/AC}$ and

Ni-CoSe₂@AC electrodes was investigated by GITT in the voltage range of 0.01–3 V (Figures S5J and S5). The results show that the D_{Na^+} of Ni-CoSe₂@TQDs/AC ($9.3 \times 10^{-11} \text{ cm}^2 \text{ s}^{-1}$) after the initial cycle is nearly four times higher than that of Ni-CoSe₂@AC ($2.4 \times 10^{-11} \text{ cm}^2 \text{ s}^{-1}$), further revealing the facilitated diffusion of Na⁺ ions benefiting from the abundant TQD sites for Na⁺ uptake.

To further visually evaluate the superiority of the two-in-one shell configuration, in situ TEM (Figure 6A) was used to study the structural stability of Ni-CoSe₂@TQDs/AC. Here, the engineered shell, as an independent protective layer for Ni-CoSe₂ species, effectively prevents the generated ultrafine products from expanding out of the nanocage for three sodiation/desodiation processes (Video S1). The representative pristine Ni-CoSe₂@TQDs/AC shows an original nanocage diameter of 671 nm (Figure 6B) and rapid volume expansion in the initial few seconds, indicating the fast Na⁺ intercalation process. After that, the diameter slightly increases to 734 nm under 4 min of sodiation due to the conversion reaction in Ni-CoSe₂@TQDs/AC,

resulting in a slight volume expansion of 9.3% (Figure 6C). Meanwhile, the particle demonstrates a volume shrinkage during the desodiation process, in which the diameter almost recovers to the pristine state once fully desodiated at 8 min (Figure 6D). During several sodiation/desodiation processes, the particle shows mild volume variation with a well-maintained structure, revealing the excellent structural stability of the TQDs/AC shell. Notably, the void space in the original particle becomes less transparent during the sodiation/desodiation processes, suggesting occupation by the generated ultrafine transition metals and Na₂Se, as well as the re-formation of Ni-CoSe₂, but with particles smaller in size (Figures 6E,F and S6). It is worth noting that the diffraction peaks of Co and Ni are not detected in ex situ XRD, while the existence of metallic Co can be proven by ex situ TEM images. This can be attributed to the amorphization and formation of ultrafine nanoparticles upon cycling and the lower content of Ni in the overall electrode, which is also consistent with other reported analyses.^{12,39} Therefore, the engineered structure

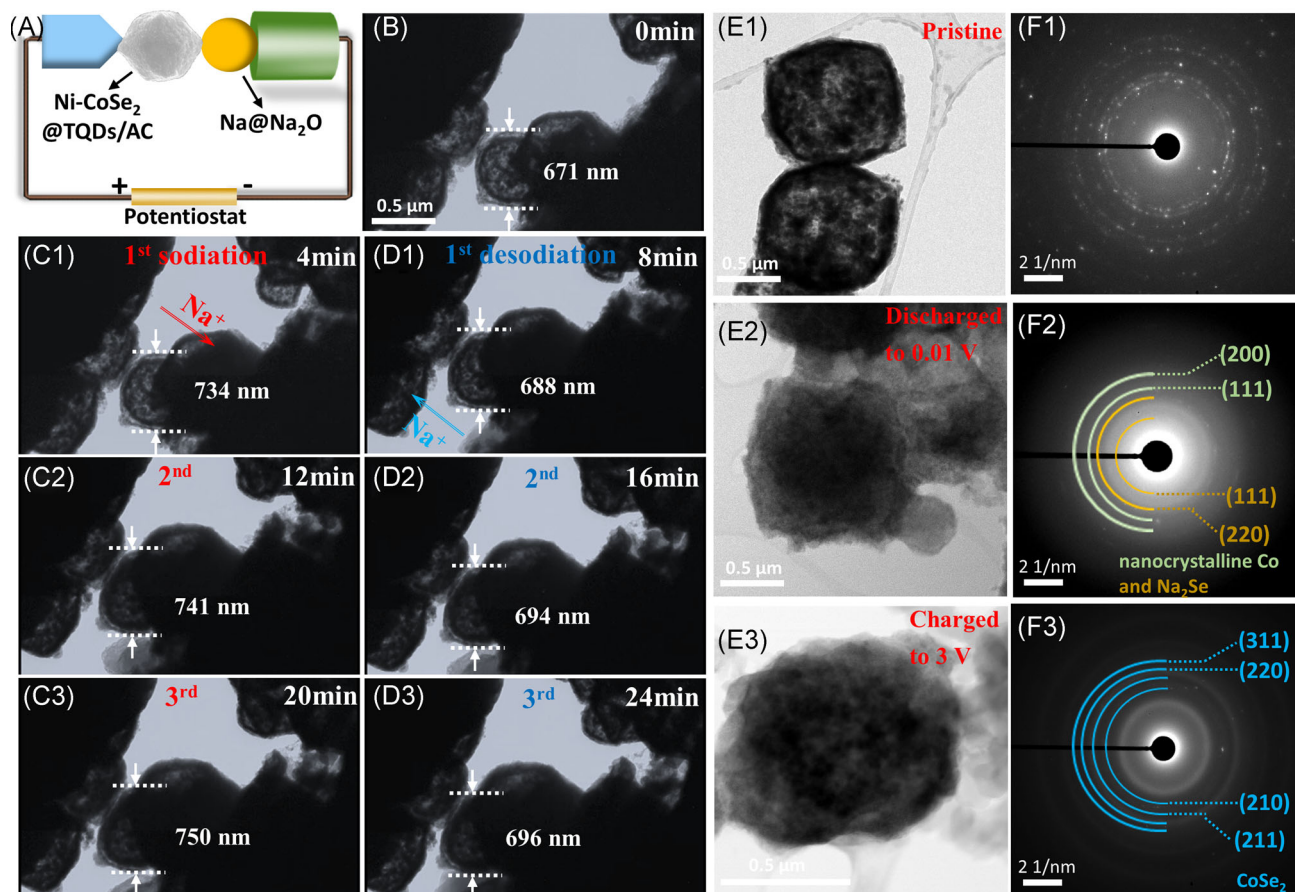


FIGURE 6 (A) Schematic illustration of the in situ transmission electron microscopy (TEM) configuration. In situ TEM observations of the (B) pristine electrode, and (C) sodiation and (D) desodiation processes for Ni-CoSe₂@TQDs/AC. (E) Ex situ TEM images and (F) corresponding selected area electron diffraction patterns of Ni-CoSe₂@TQDs/AC. TQDs/AC, titanium dioxide quantum dots/amorphous carbon hybridized shell

can not only prevent the aggregation and dissolution of ultrafine products but can also well accommodate the volume variation of the active materials during repeated charging/discharging, thus ensuring a stable cycle life. In comparison, the morphology of Ni-CoSe₂ is torn apart, and the ultrafine intermediates visibly spill out of the particle during the sodiation process (Video S2 and Figure S7). To better understand the failure of the electrode, electrochemical impedance spectroscopy measurements were then carried out. The Nyquist plots in Figure S8 show a semicircle in the high- and medium-frequency regions for all samples, corresponding to the combination of the solid–electrolyte interface film impedance and the charge-transfer impedance.^{47,48} The initial resistance of Ni-CoSe₂@TQDs/AC is lower than that of the shell-free sample, confirming its higher conductivity. Notably, the charge-transfer resistance (R_{ct}) of Ni-CoSe₂@TQDs/AC decreased to 45.7 Ω after 30 cycles, while the value for the shell-free sample increased to 286.6 Ω . When the cells were disassembled, the separator of the shell-free Ni-CoSe₂ had become very dark (Figure S9). Thus, the heavy structural damage and spilling of active materials in the shell-free sample impeded Na⁺ diffusion and electron transfer, which ultimately resulted in increased cell resistance and poor cycle life.

4 | CONCLUSION

The engineered Ni-CoSe₂@TQDs/AC that favors the transport of electrons and feasible Na⁺ uptake by integrating the advantages of titanium dioxide quantum dots and amorphous carbon has been successfully fabricated. Under the broadened voltage range of 0.01–3 V, the Ni-CoSe₂@TQDs/AC electrode shows excellent rate capability and stable cyclability compared with Ni-CoSe₂ and Ni-CoSe₂@AC electrodes, clearly demonstrating that the two-in-one shell can offer abundant TQD-active sites for sodium uptake and facilitate the diffusion of Na⁺ ions and transport of electrons. In addition, in situ and ex situ TEM visually confirmed that the structural stability of Ni-CoSe₂@TQDs/AC is mainly attributable to the TQDs/AC shell. The Ni-CoSe₂ and ultrafine reaction products can be well confined in the shell; pulverization and structural collapse of the nanocage are prevented; and the strain of volume expansion is effectively buffered, resulting in good reversible conversion between Ni-CoSe₂ and Na₂Se/Ni/Co. Overall, our present work provides a hybridized shell by coupling contents with high electronic and ionic conductivity to accommodate bimetal selenides for ultrafast sodium storage within broadened

voltage windows, which would be of huge interest for other conversion-type electrodes since they commonly suffer from volume expansion, pulverization, and escape of active material.

ACKNOWLEDGMENTS

The authors are grateful for financial support from the Fundamental Research Funds for the Central Universities (531118010111 and 531118010633) and the National Natural Science Foundation of China (52103313 and 22109041).

CONFLICT OF INTEREST

The authors declare no conflict of interest.

ORCID

Zichao Yan  <https://orcid.org/0000-0002-5640-0922>

REFERENCES

- Zhao C, Wang Q, Yao Z, et al. Rational design of layered oxide materials for sodium-ion batteries. *Science*. 2020;370(6517):708–711.
- Aslam MK, Seymour ID, Katyal N, et al. Metal chalcogenide hollow polar bipyramid prisms as efficient sulfur hosts for Na-S batteries. *Nat Commun*. 2020;11:5242.
- Hwang JY, Oh SM, Myung ST, Chung KY, Belharouak I, Sun YK. Radially aligned hierarchical columnar structure as a cathode material for high energy density sodium-ion batteries. *Nat Commun*. 2015;6:6865.
- Cao Y, Xiao L, Wang W, et al. Reversible sodium ion insertion in single crystalline manganese oxide nanowires with long cycle life. *Adv Mater*. 2011;23(28):3155–3160.
- Hu X, Liu X, Chen K, Wang G, Wang H. Core-shell MOF-derived N-doped yolk-shell carbon nanocages homogeneously filled with ZnSe and CoSe₂ nanodots as excellent anode materials for lithium- and sodium-ion batteries. *J Mater Chem A*. 2019;7(18):11016–11037.
- Sun T, Zhao X, Li B, et al. NiMoO₄ nanosheets anchored on N-S doped carbon clothes with hierarchical structure as a bidirectional catalyst toward accelerating polysulfides conversion for Li-S battery. *Adv Funct Mater*. 2011;31(25):2101285.
- Zhang SS. The redox mechanism of FeS₂ in non-aqueous electrolytes for lithium and sodium batteries. *J Mater Chem A*. 2015;3(15):7689–7694.
- Kitajou A, Yamaguchi J, Hara S, Okada S. Discharge/charge reaction mechanism of a pyrite-type FeS₂ cathode for sodium secondary batteries. *J Power Sources*. 2014;247:391–395.
- Ge P, Hou H, Li S, Huang L, Ji X. Three-dimensional hierarchical framework assembled by cobblestone-like CoSe₂@C nanospheres for ultrastable sodium-ion storage. *ACS Appl Mater Interfaces*. 2018;10(17):14716–14726.
- Zhou K, Han Y, Tang D, et al. Hierarchical N-doped HMCN/CNT hybrid carbon frameworks assembling cobalt selenide nanoparticles for advanced properties of lithium/sodium storage. *Adv Mater Interfaces*. 2020;7(2):1901699.
- Xiao Y, Zhang J, Su D, et al. In-situ growth of V-shaped CoSe₂ nanorods on graphene with C–Co bonding for high-rate and

- long-life sodium-ion batteries. *J Alloys Compd.* 2020;819:153359.
12. Ou X, Liang X, Zheng F, et al. In situ X-ray diffraction investigation of CoSe₂ anode for Na-ion storage: effect of cut-off voltage on cycling stability. *Electrochim Acta.* 2017;258:1387-1396.
 13. Wang X, Li F, Li W, Gao W, Tang Y, Li R. Hollow bimetallic cobalt-based selenide polyhedrons derived from metal-organic framework: an efficient bifunctional electrocatalyst for overall water splitting. *J Mater Chem A.* 2017;5(34):17982-17989.
 14. Zhang K, Park M, Zhou L, et al. Urchin-like CoSe₂ as a high-performance anode material for sodium-ion batteries. *Adv Funct Mater.* 2016;26(37):6728-6735.
 15. Jiang Y, Zou G, Hou H, et al. Composition engineering boosts voltage windows for advanced sodium-ion batteries. *ACS Nano.* 2019;13(9):10787-10797.
 16. Yousaf M, Chen Y, Tabassum H, et al. A Dual protection system for heterostructured 3D CNT/CoSe₂/C as high areal capacity anode for sodium storage. *Adv Sci.* 2020;7(5):1902907.
 17. Li Z, Fang Y, Zhang J, Lou XWD. Necklace-like structures composed of Fe₃N@C yolk-shell particles as an advanced anode for sodium-ion batteries. *Adv Mater.* 2018;30(30):1800525.
 18. Huang H, Xu R, Feng Y, et al. Sodium/potassium-ion batteries: boosting the rate capability and cycle life by combining morphology, defect and structure engineering. *Adv Mater.* 2020;32(8):1904320.
 19. Hu Z, Liu Q, Chou SL, Dou SX. Advances and challenges in metal sulfides/selenides for next-generation rechargeable sodium-ion batteries. *Adv Mater.* 2017;29(48):1700606.
 20. Lynch BB, Kelliher AP, Anderson BD, et al. Sulfidation and selenidation of nickel nanoparticles. *Carbon Energy.* 2021;3(4):582-589.
 21. Kang SH, Jang JK, Jeong HY, et al. Polyacrylonitrile/phosphazene composite-based heat-resistant and flame-retardant separators for safe lithium-ion batteries. *ACS Appl Energy Mater.* 2022;5(2):2452-2461.
 22. Qin X, Kim D, Piao Y. Metal-organic frameworks-derived novel nanostructured electrocatalysts for oxygen evolution reaction. *Carbon Energy.* 2021;3(1):66-100.
 23. Wu T, Zhang W, Yang J, et al. Architecture engineering of carbonaceous anodes for high-rate potassium-ion batteries. *Carbon Energy.* 2021;3(4):554-581.
 24. Zhu Y, Hu A, Tang Q, et al. Compact-nanobox engineering of transition metal oxides with enhanced initial coulombic efficiency for lithium-ion battery anodes. *ACS Appl Mater Interfaces.* 2018;10(10):8955-8964.
 25. Yu J, Xiao J, Li A, et al. Enhanced multiple anchoring and catalytic conversion of polysulfides by amorphous MoS₃ nanoboxes for high-performance Li-S batteries. *Angew Chem Int Ed.* 2020;59(31):13071-13078.
 26. Fang Y, Luan D, Chen Y, Gao S, Lou XWD. Rationally designed three-layered Cu₂S@Carbon@MoS₂ hierarchical nanoboxes for efficient sodium storage. *Angew Chem Int Ed.* 2020;132(18):7245-7250.
 27. Zhang H, Huang X, Noonan O, Zhou L, Yu C. Tailored yolk-shell Sn@C nanoboxes for high-performance lithium storage. *Adv Funct Mater.* 2017;27(8):1606023.
 28. Lu P, Sun Y, Xiang H, Liang X, Yu Y. 3D amorphous carbon with controlled porous and disordered structures as a high-rate anode material for sodium-ion batteries. *Adv Energy Mater.* 2018;8(8):1702434.
 29. Liu J, Xia H, Xue D, Liu L. Double-shelled nanocapsules of V₂O₅-based composites as high-performance anode and cathode materials for Li ion batteries. *J Am Chem Soc.* 2009;131(34):12086-12087.
 30. Wang D, Zhang W, Drewett NE, et al. Exploiting anti-T-shaped graphene architecture to form low tortuosity, sieve-like interfaces for high-performance anodes for Li-based cells. *ACS Cent Sci.* 2018;4(1):81-88.
 31. Zhang W, Wang D, Zheng W. A semiconductor-electrochemistry model for design of high-rate Li ion battery. *J Energy Chem.* 2020;41:100-106.
 32. Zhao B, Liu Q, Wei G, et al. Synthesis of CoSe₂ nanoparticles embedded in N-doped carbon with conformal TiO₂ shell for sodium-ion batteries. *Chem Eng J.* 2019;378:122206.
 33. Ma Y, Zhang L, Cai Z, et al. Study of TiO₂-coated α -Fe₂O₃ composites and the oxygen-defects effect on the application as the anode materials of high-performance Li-ion batteries. *ACS Appl Energy Mater.* 2020;3(12):11666-11673.
 34. Chen C, Wen Y, Hu X, et al. Na⁺ intercalation pseudocapacitance in graphene-coupled titanium oxide enabling ultra-fast sodium storage and long-term cycling. *Nat Commun.* 2015;6:6929.
 35. Zhou W, Lu J, Zhou K, et al. CoSe₂ nanoparticles embedded defective carbon nanotubes derived from MOFs as efficient electrocatalyst for hydrogen evolution reaction. *Nano Energy.* 2016;28:143-150.
 36. Tang Y, Zhao Z, Hao X, et al. Engineering hollow polyhedrons structured from carbon-coated CoSe₂ nanospheres bridged by CNTs with boosted sodium storage performance. *J Mater Chem A.* 2017;5(26):13591-13749.
 37. Luo W, Wang Y, Chou S, et al. Critical thickness of phenolic resin-based carbon interfacial layer for improving long cycling stability of silicon nanoparticle anodes. *Nano Energy.* 2016;27:255-264.
 38. Yeo Y, Jung JW, Park K, Kim ID. Graphene-wrapped anatase TiO₂ nanofibers as high-rate and long-cycle-life anode material for sodium ion batteries. *Sci Rep.* 2015;5:13862.
 39. Fang G, Wang Q, Zhou J, et al. Metal organic framework-templated synthesis of bimetallic selenides with rich phase boundaries for sodium-ion storage and oxygen evolution reaction. *ACS Nano.* 2019;13(5):5635-5645.
 40. Kwak IH, Im HS, Jang DM, et al. CoSe₂ and NiSe₂ nanocrystals as superior bifunctional catalysts for electrochemical and photoelectrochemical water splitting. *ACS Appl Mater Interfaces.* 2016;8(8):5327-5334.
 41. Brutti S, Gentili V, Menard H, Scrosati B, Bruce PG. TiO₂-(B) nanotubes as anodes for lithium batteries: origin and mitigation of irreversible capacity. *Adv Energy Mater.* 2012;2(3):322-327.
 42. Tabassum H, Zhi C, Hussain T, Qiu T, Aftab W, Zou R. Encapsulating trogtalite CoSe₂ nanobuds into BCN nanotubes as high storage capacity sodium ion battery anodes. *Adv Energy Mater.* 2019;9(39):1901778.
 43. Fang Y, Yu XY, Lou XWD. Formation of hierarchical Cu-doped CoSe₂ microboxes via sequential ion exchange for high-performance sodium-ion batteries. *Adv Mater.* 2018;30(21):1706668.

44. Li B, Liu Y, Jin X, et al. Designed formation of hybrid nanobox composed of carbon sheathed CoSe₂ anchored on nitrogen-doped carbon skeleton as ultrastable anode for sodium-ion batteries. *Small*. 2019;15(42):1902881.
45. Xia Q, Liang Y, Lin Z, et al. Confining ultrathin 2D superlattices in mesoporous hollow spheres renders ultrafast and high-capacity Na-ion storage. *Adv Energy Mater*. 2020; 10(36):2001033.
46. Zhou L, Zhang K, Sheng J, et al. Structural and chemical synergistic effect of CoS nanoparticles and porous carbon nanorods for high-performance sodium storage. *Nano Energy*. 2017;35:281-289.
47. Yan Z, Tian Q, Liang Y, et al. Electrochemical release of catalysts in nanoreactors for solid sulfur redox reactions in room-temperature sodium-sulfur batteries. *Cell Rep Phys Sci*. 2021;2(8):100539.
48. Guo Q, Ma Y, Chen T, et al. Cobalt sulfide quantum dot embedded N/S-doped carbon nanosheets with superior

reversibility and rate capability for sodium-ion batteries. *ACS Nano*. 2017;11(12):12658-12667.

SUPPORTING INFORMATION

Additional supporting information can be found online in the Supporting Information section at the end of this article.

How to cite this article: Yan Z, Zhao L, Liang Y, et al. Two-in-one shell configuration for bimetal selenides toward fast sodium storage within broadened voltage windows. *Carbon Energy*. 2022;4:586-597. doi:10.1002/cey2.197